High-pressure, halogen-bearing melt preserved in ultrahigh-temperature felsic granulites of the Central Maine Terrane, Connecticut (U.S.A.)

Silvio Ferrero, Jay Ague, Patrick O'brien, Bernd Wunder, Laurent Remusat, Martin A Ziemann, Jennifer Axler, Patrick J O'Brien

HAL Id: hal-03402462
https://hal.science/hal-03402462v1

Submitted on 25 Oct 2021

1   **High pressure, halogen-bearing melt preserved in ultra-high temperature felsic granulites**

2   **of the Central Maine Terrane, Connecticut (US)**

3   Silvio Ferrero[1,2], Jay Ague[3], Patrick J. O'Brien[1], Bernd Wunder[4], Laurent Remusat[5], Martin A.

4   Ziemann[1], Jennifer Axler[6]

5

6   *[1] Universität Potsdam, 14476 Potsdam, Germany*

7   *[2] Museum für Naturkunde (MfN), Leibniz-Institut für Evolutions-und Biodiversitätsforschung,*

8   *10115 Berlin, Germany*

9   *[3] Yale University, New Haven, CT, 06520-8109, US*

10   *[4] Helmholtz-Zentrum Potsdam, GFZ, D-14473 Potsdam, Germany*

11   *[5]Museum National d'Histoire Naturelle, Paris*

12   *[6] Wellesley College, 106 Central Street – Wellesley, MA 02481*

13

14   **Abstract**

15   Inclusions of high pressure melts provide crucial information on the fate of crustal rocks in the

16   deep roots of collisional orogens during collision and crustal thickening, often at rather extreme

17   conditions, e.g. temperatures in excess of 1000°C. However, findings of this type are still a

18   relative rarity among case studies of MI in metamorphic rocks. Here we present the results of the

19   experimental and microchemical investigation of nanogranitoids in garnets from the felsic

20   granulites of the Central Maine Terrane (Connecticut, US). Their successful experimental re-

21   homogenization at almost 2 GPa confirms that they originally were trapped portions of deep

22   melts and makes them the first direct evidence of high pressure during peak metamorphism and

23   melting for these felsic granulites. The trapped melt has a hydrous, granitic and peraluminous

1

24 character typical of crustal melts from metapelites. This melt is higher in mafic components (FeO

25 and MgO) than most of the nanogranitoids investigated so far, likely the result of the extreme

26 melting temperatures – well above 1000°C. This is the first natural evidence of the positive

27 correlation between temperature and mafic character of the melt, a trend previously supported

28 only by experimental evidence. Moreover it poses a severe *caveat* against the common

29 assumption that partial melts from metasediments at depths are always leucogranitic in

30 composition.

31 NanoSIMS measurement on re-homogenized inclusions show significant amounts of CO_2, Cl and

32 F. Halogens abundance in the melt is considered a proxy for the presence of brines, strongly

33 saline fluids, at depth. Brines are known to shift the melting temperatures of the system toward

34 higher values, and may have been responsible for delaying melt production via biotite

35 dehydration melting until these rocks reached extreme temperatures of more than 1000°C, rather

36 than 800-850°C as commonly observed for these reactions.

37   **Keywords**

38   High pressure granulites, anatexis, nanogranitoids, carbon, halogens, piston cylinder

39

INTRODUCTION

41   The investigation of melt inclusions in felsic (Ferrero et al., 2015; Cesare et al., 2015) and

42   mafic (Ferrero et al., 2018a) granulites is the most straightforward approach to the investigation

43   of melting processes in the lower continental crust, directly in their source region. These droplets

44   of anatectic melt are generally partially to totally crystallized, i.e. as nanogranitoids due to the

45   slow cooling of the host rock (Ferrero et al., 2012; Cesare et al., 2015). They contain a

46   cryptocrystalline aggregate of phases consistent with the crystallization of a silicate rich melt

47   (Ferrero et al., 2018b). The expected phases include, but they are not limited to, OH-bearing

48   phases, quartz and feldspar(s) or their metastable polymorphs (Ferrero et al., 2016). Just like fluid

49   and mineral inclusions, melt inclusions in metamorphic rocks are tools for natural scientists to

50   peer into the history of the host rocks, obtain geochemical information on deep processes, and to

51   better constrain P-T-t-X history of the rock (Ferrero and Angel, 2018).

52   Multiphase inclusions with features consistent with nanogranitoids were reported by Ague and

53   Axler (2015) in garnets from layers of sillimanite-rich rocks hosted in gneisses of the Central

54   Maine Terrane (CMT - Acadian orogeny, NE Connecticut, US). Phase assemblages in the

55   inclusions and microstructures classify them as former droplets of melt trapped during garnet

56   formation at the metamorphic peak, ~1050°C and ≥1 GPa (Axler and Ague, 2015). The host rock

57   has attracted considerable interest in recent years because of its very high T of re-equilibration at

58   relatively low P (including cordierite-spinel assemblages), allowing Ague et al. (2013) to

59   interpret them as the first example of ultrahigh temperature (*UHT*) metamorphic rocks in North

60   America. By definition, *UHT* metamorphism involves T in excess of 900°C achieved along

61   apparent geothermal gradient ≥20°C/Km (Brown, 2006), i.e. mostly in the stability field of

62   sillimanite. *UHT* metamorphism has been to date identified in dozens of localities worldwide,

63   mostly in Precambrian rocks (Kelsey, 2008), although much younger *UHT* rocks, i.e. Miocene in

64   age, have been also recently reported (Pownall et al., 2018). More recent studies of other rocks in

65   the CMT document high-pressure granulite facies metamorphism (~1050 °C, ~1.8 GPa) of silica-

66   undersaturated garnet-spinel-corundum gneisses (Keller and Ague, 2018), as well as UHP

67   metamorphism (Keller and Ague, 2020).

68   Piston cylinder re-homogenization followed by in situ characterization is a common and well-

69   established approach for nanogranitoids studies to follow in order to (1) prove that they originally

70   were indeed droplets of melt, and (2) characterize geochemistry and fluid content and speciation

71   content of anatectic melt (e.g. Acosta-Vigil et al., 2016; Bartoli et al., 2016; Carvalho et al., 2018;

72   Bartoli et al., 2019). Our detailed experimental and microchemical work confirmed that the CMT

73   multiphase inclusions were originally a hydrous and halogen-rich granitic melt formed at T in

74   excess of 1000°C, the hottest preserved melt so far found in natural metasedimentary protolith.

75   Our approach leads to surprising outcomes with broad significance in terms of melt composition

76   and melting processes in the deepest parts of orogenic root zones, as well as of regional

77   geodynamic evolution.

78   **METHODS**

79   Our study involved the use of a piston cylinder press, back-scattered-electron (BSE) imaging,

80   electron probe analyses (EPMA), energy-dispersive-spectrometry (EDS) elemental mapping and

81   micro-Raman spectroscopy. Several garnet chips with unexposed nanogranitoids of both equant

82   and tubular shape were manually separated from doubly-polished thick sections and used as

83   starting material in re-homogenization experiments. The chips were loaded in a platinum capsule

84   then filled with silica powder, without adding water. The capsules were kept at in a Johannes-

85   type piston-cylinder apparatus at GFZ-Potsdam at variable T and P conditions for up to 24 hours.

86   The temperature in the capsule was controlled using a Type S thermocouple (Pt-PtRh10) with a

87    $\pm 10\ °C$ uncertainty, while the accuracy of the pressure (P) measurement is estimated to be ± 0.05

88   GPa. Quenching of the experimental charge took place at high P, and the machine was unloaded

89   only after reaching ambient temperature. In-situ analyses were then performed on capsules

90   mounted in epoxy and polished to expose re-homogenized inclusions (for further details see

91   Bartoli et al. 2013b; Ferrero et al. 2015).

92   The Field Emission Gun electron microprobe (FEG-EMP) JEOL Hyperprobe JXA-8500F

93   available at the Natural History Museum of Berlin was used to acquire high-resolution BSE

94   images and EDS elemental maps on nanogranitoids and re-homogenized inclusions. The glass

95   resulting from re-homogenization was analyzed using a JEOL JXA-8200 EMP at Potsdam

96   University. Analytical conditions were similar to previous studies of nanogranitoids (Ferrero et

97   al. 2012; 2015) at 15 kV, 3.5 nA and beam diameter of 1 μm to avoid contamination from the

98   surrounding host. Alkali loss correction factors were estimated using haplogranitic standards

99   (Morgan and London, 2005) and are in the range 17-23% relative for Na_2O and 10-13 % relative

100   for K_2O depending on the analytical session.

101   Fluorine, CO_2, and H_2O analyses were performed via Nano Secondary Ion Mass Spectrometry

102   (NanoSIMS) using the Cameca NanoSIMS 50 operated at the Muséum National d'Histoire

103   Naturelle of Paris following the procedure described in Bartoli et al. (2014) and Créon et al.

104   (2018). Polished capsules with re-homogenized inclusions on the garnet surface were mounted in

105   Indium along with standard glasses, and the inclusions identified through images of $^{28}Si^{-}$ and

106   $^{56}Fe^{16}O^{-}$ secondary ions. Pre-sputtering on a $5 \times 5\ \mu m^2$ surface area for 2 min preceded each

107   analysis in order to remove gold coating, surface contamination and achieve a steady-state

108   sputtering regime. A 20 pA Cs^{+} primary beam was used for data acquisition via rastering of a 3×3

109   μm^2 surface area. Ions were exclusively collected from the inner 1×1 μm^2 (using the beam

110   blanking mode) to minimize surface contamination. Each analysis comprised 200 cycles with a

111   duration of 1.024 s. Secondary ions of $^{12}C^-$, $^{16}OH^-$ (proxy for H_2O), ^{19}F, $^{28}Si^-$ and $^{56}Fe^{16}O^-$ were

112   recorded simultaneously in multicollection mode, using electron multipliers with a dead time of

113   44 ns. Mass resolution was set to 5500 to resolve any mass interference on the selected ions. Only

114   analyses with a stable $^{16}OH^-/^{28}Si^-$ ratio were considered in this study. Three glasses of

115   leucogranitic composition and known concentrations of H_2O, varying between ~0.3 and 4.86

116   wt% were used for calibration (see Supplementary material). For F concentration, we used NIST

117   610 and 612 standards to determine $[F]/[SiO_2]$ ratios from $^{19}F^-/^{28}Si^-$. Four trachyandesitic

118   standards (STR 9, 10, 11 and 13) were used to correct for carbon measurements (Créon et al.,

119   2018): these are glass fragments of shoshonite lava from the Stromboli volcano that were

120   experimentally doped in carbon and water by Bureau et al. (2003). Analytical uncertainty on each

121   NanoSIMS measurement (based on the Poisson error due to counting statistics) was combined

122   with the uncertainty on the calibration (corresponding to 66% interval of confidence) by

123   quadratic sum to obtain the 66% uncertainty on values reported in Table 3.

124   Micro-Raman spectroscopy was performed using a HORIBA Jobin Yvon LabRAM HR 800

125   located at the Institute of Geoscience, University of Potsdam. An air-cooled Nd:YAG laser was

126   used for excitation (λ = 532 nm, laser power on the sample of 2–3 mW) with a grating of 300

127   lines/mm, slit width and confocal hole set to 100 μm and 200 μm, respectively. The Raman

128   spectra of re-homogenized glass inclusions as well as crystal phases were acquired with a 100×

129   objective in the wavenumber range 100–4000 cm^{-1}, integrating 3 repetitions of 60 s with spectral

130   resolution of 10 cm^{-1}. Raman maps were obtained integrating 2 repetitions of 30 s in 4 spectral

131 windows on each point of the mapped area. Different phases were visualized in the map by color

132 coding of the indexed Raman bands of the phases (cf. O'Brien & Ziemann, 2008).

133

134   **PETROGRAPHIC FEATURES OF THE STARTING MATERIAL**

135   The host rocks are rusty schists characterized by the assemblage garnet+sillimanite+K-

136 feldspar+plagioclase+quartz+cordierite+biotite (Fig.1a). The sillimanite is commonly found as

137 pseudomorphs after kyanite. Detailed information on sample location and petrographic features

138 are in Axler and Ague (2015). The inclusions occur in the inner part of garnet porphyroblasts

139 with a random distribution indicative of a primary nature, i.e. they formed during growth of the

140 host garnet (Fig. 1b; see also Ferrero et al., 2012). They vary in shape from isometric with

141 diameter ≤10 μm (Fig. 1c) to needles with length ≤100 μm and few μm across (Fig. 1d). The

142 latter type is by far the most common in each cluster, a shape never before observed in such

143 abundance in case studies of nanogranitoid, more commonly isometric (Ferrero et al., 2018b;

144 Cesare et al., 2015). The most elongated inclusions show often cracks of limited extension at the

145 corners, evidence of decrepitation. The detailed microchemical and microstructural investigation

146 of the inclusions performed by Axler and Ague (2015) showed that, before the experimental runs,

147 they contain a rather constant assemblage consisting of quartz, phlogopite, white mica and, very

148 often, a compositionally variable phase (CV phase in Axler and Ague 2015) interpreted as

149 residual glass.

150   Raman investigation (Fig. 2a) and mapping of isometric inclusions shows that cristobalite is

151 present instead of quartz in some inclusions (Fig. 2b) and coexists with two micas and accessory

152 phases such as apatite and ilmenite (Fig. 2c, d, e), whereas no inclusion show the presence of

153 residual glass. However, the Raman map shows a crystalline phase with main peaks at 292, 430

7

154 and 479 cm^{-1}, assigned to a still unidentified and possibly new phase (hence "phase 430") already

155 found and analyzed in nanogranitoids from HP/UHP rocks of the Bohemian Massif, and having

156 composition similar to a granitic glass. Graphite occurs as mineral inclusions in garnet and

157 occasionally as a trapped phase in the inclusions. A prominent feature of the host garnet is the

158 presence of abundant rutile and ilmenite needles dominantly oriented parallel to <111> of garnet.

159 Interestingly, needle-shaped nanogranitoids are oriented in the same directions, and typically

160 contain rutile and /or ilmenite as trapped phases.

161 **RESULTS**

162 Multiple re-homogenization experiments were performed at T=1050°C and variable confining

163 P, in the range 1.0 – 2.0 GPa (details on experimental runs and products are in Table 1; P-T

164 conditions of each experiment are summarized in Fig. 3). The experimental conditions were

165 chosen to be as close as possible to the conditions of formation, estimated to be ≈1040°C based

166 on Zr-in-Rt thermometry on the rutile needles present along with nanogranitoids in the garnet

167 core (Axler and Ague, 2015). The T estimates were calculated assuming 1 GPa as formation P of

168 the host garnet and melt entrapment, thus representing a minimum value (Ague et al., 2013).

169 Each experiment shows complete re-melting of the inclusions, i.e. no leftovers of the original

170 phases in the nanogranitoids are visible after the heating run, with the exception of clearly

171 trapped accessories such as rutile and ilmenite. The absence of embayments and regular linear

172 walls in the inclusions rules out that garnet dissolved into the melt (Ferrero et al., 2012; Bartoli et

173 al., 2013), as expected in case of significant overheating during the experiments, i.e. the chosen

174 temperature is likely very close to the liquidus of the trapped melt. However, the experiments

175 performed at P <1.7 GPa (numbers 1, 2 in fig. 3) constantly show formation of new garnet,

176 higher in Mg than the original host phase (Figs. 4a,b,c,d) and occasionally small orthopyroxene

177   crystals identified via Raman spectroscopy at P ≤1.2 GPa. Moreover, at 1 GPa most inclusions

178   show extensive evidence of decrepitation (Fig. 4a). The two experiments performed at 1.7 and

179   2.0 GPa (numbers 3 and 4 respectively, Fig. 3) do show fully re-homogenized glassy inclusions

180   without evidence of decrepitation and/or formation of new phases (Figs. 4e,f,g,h,i).

181

182   **Melt composition**

183   The glass measured in the inclusions after successful experimental re-homogenization is

184   hydrous, granitic (Fig. 5a,b) and very K-rich (av. K_2O/Na_2O= 3.89, Table 2), with a clear

185   peraluminous (ASI=1.22, Fig. 6c) and alkalic to alkali-calcic character (Fig. 5d). Importantly,

186   such melts are not leucogranitic, as commonly expected for anatectic melts from melting of

187   metasediments: they have indeed a rather high FeO+MgO content (4.05 wt%; 4.27 wt% when

188   recalculated on an anhydrous basis; Table 2). The presence of H_2O in the glass is visible in

189   Raman spectra acquired on re-homogenized nanogranitoids, which show the broad band of water

190   in the region 3200-3800 cm^{-1} (Fig. 6).

191   The H_2O content of the melt, along with CO_2 and F, was measured in garnets from experiment

192   #3 and #4 using NanoSIMS. One single inclusion shows very low values of all three volatile

193   species, suggesting that it may have lost most of its volatiles possibly as result of decrepitation

194   during quenching (measurement Exp3_MI_1 in Table 3) and thus it is not further considered in

195   the average values calculated below. The volatiles were quantified as 4.40 wt% H_2O, 3072 ppm

196   CO_2 and 3161 ppm F on average (Fig.7a). With the exclusion of the single analysis discussed

197   above, H_2O content in the rest of the dataset is rather consistent (Fig. 7a), whereas the CO_2 and F

198   contents of the melt vary by an order of magnitude (Figure 7a; Table 3) depending on the

199   inclusion (Fig. 7b, c). Interestingly, EMPA measurements on the re-homogenized inclusions

200 show that Cl is also present in remarkable amounts, reaching almost 1 wt%, with average 0.32

201 wt%, making this melt more enriched in halogens (Cl, F) than any previous anatectic melt so far

202 investigated in nanogranitoids.

203

204   **DISCUSSION**

205   The present study targets polycrystalline inclusions in garnet form felsic granulites of the

206 Central Maine Terrane. Our results confirm that they are volumes of crystallized melt trapped

207 during garnet growth at the metamorphic peak, as already proposed based on mineralogical and

208 microstructural investigation by Axler and Ague (2015). Raman investigation shows the presence

209 of metastable cristobalite, i.e. formed outside its stability field (see e.g. Hwang et al., 2004). The

210 occurrence of metastable polymorphs in nanogranitoids has been interpreted as direct evidence

211 that the inclusions preserve their original composition, as these phases recrystallize to their most

212 common counterparts (i.e. quartz) when the inclusions decrepitates, i.e. becomes an open system,

213 able to exchange components with the rock matrix via cracks in the host garnet (Ferrero et al.,

214 2016). Such inclusions therefore offer access to unaltered deep melts still preserved in the natural

215 rock which underwent melting at depth (Ferrero and Angel, 2018).

216   The investigation of CMT nanogranitoids thus provides a detailed portrait of formation

217 conditions, geochemistry, and volatile content of melt from metasediments at crustal depth. The

218 extremely high T at which the melt was produced is rather close to the Bt-out curve according to

219 the melting experiments on metasediments of Auzeanneau et al. (2006). Indeed the peraluminous

220 and granitic nature of the re-homogenized melt, its relatively low amount of H_2O and its

221 occurrence in (peritectic) garnet are all features consistent with melt generated by biotite

222 dehydration melting (LeBreton and Thompson, 1988), with residual biotite still locally visible as

10

223   mineral inclusions (Fig. 1a). Furthermore, the enrichment in chlorine and fluorine of the trapped

224   melt is likely to influence the stability of the biotite (see discussion in the paragraph "volatiles in

225   high pressure melt").

226   The composition measured in the re-homogenized inclusions, especially its granitic character

227   and the high K/Na ratio (≈4:1) is consistent with the phase assemblage, which always includes

228   quartz/cristobalite plus two K-bearing phases (muscovite and phlogopite). The phase 430

229   identified via Raman investigation is likely to be the "phase CV", reported in these inclusions by

230   Axler and Ague (2015) and interpreted as residual glass because of their granitic-like

231   composition: the narrow peaks visible in its Raman spectrum however clearly belongs to a

232   crystalline rather than a glass phase. Moreover, very similar compositions to the one reported by

233   Ague and Axler (2015) were measured in phase 430 from garnet pyroxenites from the

234   Granulitgebirge (Bohemian Massif; unpublished EMP data; Ferrero et al., in preparation), thus

235   making this phase the main Na repository in the targeted nanogranitoids.

236   A peculiarity of this case study is represented by the shape of the inclusions. Most case studies

237   of nanogranitoids show inclusions with a more or less developed negative crystal shape, the

238   response of host garnet to the need of lowering the surface free energy of the melt-garnet

239   interface and move toward textural equilibration (Ferrero et al., 2012). Instead tubular/acicular

240   shapes in nanogranitoids are not unheard of (Ferrero et al, 2012; Cesare et al., 2015) but they are

241   overall a rarity. CMT nanogranitoids are a rather unique case as the acicular shape, i.e. defined by

242   an extreme elongation/width ratio, characterizes the majority of the inclusions (Fig. 1b,c). So far

243   only the polycrystalline inclusions in the garnet megacrysts of Gore Mountain in the Adirondacks

244   (Darling et al., 1997) show similar features, although in the latter case only ~50% of the

245   inclusions have such shape (Ferrero and Angel, 2018). Further investigations are needed to

246 understand the reasons underlying the dichotomy negative-crystal versus acicular shape in

247 inclusions from different localities.

248 The original rationale at the base of our work was two-folds: verifying the former melt nature

249 of the inclusions and obtaining the bulk composition of the original melt. The study however

250 generated three most unexpected results: (a) re-homogenization experiments show that this melt

251 formed under high pressure (*HP*) conditions, in contrast with previous studies of these felsic

252 granulites; (b) whereas the melt itself is peraluminous and granitic in composition, rather

253 common features in melts from metasediments, it shows an unexpected high mafic (FeO+MgO)

254 component; (c) in terms of volatiles, the melt contains significant amounts of halogens (Cl, F)

255 besides typical species observed in silicate melts, e.g. H_2O and CO_2.

256

257 **First evidence of *HP* in the felsic granulites of the Central Maine Terrane**

258 Possibly the most consequential result of our study is that the inclusions re-homogenize

259 completely in equilibrium with the host garnet only at $P \geq 1.7$ GPa, considerably in excess of the

260 minimum of 1.0 GPa as originally expected based on the estimates of Ague et al. (2013) and

261 Axler and Ague (2015). Garnet growth conditions and thus MI entrapment coincide with those of

262 partial melting, as both garnet and melt are products of the same melting reaction (Cesare et al.,

263 2015 and references therein), and are under chemical equilibrium during their formation. Thus,

264 successful re-homogenization experiments on nanogranitoids are a completely independent tool

265 to constrain the PT conditions of garnet formation in presence of melt (Ferrero et al., 2018b).

266 Both *P* and *T* still need to be calculated beforehand using independent methods, e.g.

267 thermodynamic modeling and classic geothermobarometry on the metamorphic assemblage to

268 which the inclusion-bearing garnet belongs, in order to proceed with the experiments. If the

269 calculated formation conditions are correct, (most of) the nanogranitoids should re-melt

270 completely without reacting with the host during the experimental run (see Bartoli et al. 2013a,b;

271 Acosta-Vigil et al., 2016; Ferrero et al., 2015; 2016; 2018b; Borghini et al. 2018). Conversely,

272 textural evidence of melt-garnet disequilibrium as well as decrepitation evidence would indicate

273 the experimental parameters were not representative of the formation conditions. As an example,

274 the critical evaluation of the nanogranitoid microstructures after heating experiments at different

275 P allowed Ferrero et al. (2018b) to bracket the P conditions of melting of the felsic granulites of

276 Orlica–Śnieżnik Dome (OSD; Bohemian Massif) to 2.7 ±0.1 GPa, starting from an initial range

277 of calculated P spanning from 1.8 to 3.0 GPa based on previous geothermobarometric and

278 modelling studies.

279 Our detailed experimental work on the CMT nanogranitoids shows that the nanogranitoids re-

280 melt at T=1050°C. At 1.0 GPa the abundance of decrepitation cracks in the re-melted inclusions

281 is a clear evidence of insufficient confining P, which leads to failure of the container (the garnet)

282 due to inclusion overpressurization during the heating run. Moreover, all the experiments at P

283 <1.7 GPa show evidence of chemical disequilibrium between the newly produced glass and the

284 surrounding garnet. This causes melt-garnet interaction, with formation of new phases not present

285 in the inclusions before experimental runs, e.g. orthopyroxene and/or change in composition

286 (Mg-increase) of the garnet around the inclusion. Newly formed, Mg-richer garnet was also

287 reported in nanogranitoids from the OSD felsic granulites after experiments at P lower than those

288 of melt formation (Ferrero et al., 2018). Hence the microstructural appearance of the CMT

289 nanogranitoids after reheating show an evolution similar to that reported in Ferrero et al. (2018b),

290 with the Mg-rich garnet disappearing once the confining P reaches 1.7 GPa, thus suggesting that

291 both garnet and melt formed at P ≥1.7 GPa.

High mafic content in pristine anatectic melt from metasediments

Granitic melts with geochemistry similar to the CMT nanogranitoids, i.e., high ASI index, rather high normative orthoclase and high FeO+MgO, are reported from experiments on natural metapelitic rocks at 1 GPa and 1025-1075 °C (Patiño-Douce and Johnston, 1991) and in nanogranitoid from metapelitic migmatites which experienced UHT conditions, 950°C and 0.5 GPa, in the Kerala Khondalite Belt, Southern India (Cesare et al., 2009; Ferrero et al., 2012; see table 2 and fig. 8a,b for the whole nanogranitoid and experimental dataset). It may be argued that such a mafic-rich character is the result of contamination between glass and host, as the inclusions are hosted in Fe- and Mg-rich garnet (Axler and Ague, 2015). However, contamination via (even limited) dissolution of garnet during re-heating experiments can be excluded based on microstructural basis, i.e. the inclusions show regular shapes and lack embayments indicative of melt-garnet interaction. Contamination during EMPA analysis can be also ruled out for the inclusions selected for EMPA investigation and reported in Table 2. The size of the re-homogenized inclusions was sufficiently large (>5 µm in diameter) to avoid the excitation volume created by the electron beam (diameter 1 µm) to come in contact with the host. In the few cases where the inclusions were ≤5 µm, garnet contamination was clearly visible as the measured SiO_2 showed a sharp decrease, coupled with FeO increase (Fig. 8a). As microstructural evidence of garnet dissolution was completely absent from these small inclusions, we ascribed this phenomenon to the fact that the excitation volume created by the beam also included a portion of the host. Analyses from inclusions below 4-5 µm were then removed from the dataset (contaminated analyses are given in the supplementary material). Based on such considerations,

314 the high mafic component of the melt preserved in these felsic granulites should be considered a

315 primary feature.

316   CMT nanogranitoids have a very high average FeO+MgO content when compared with

317 experimental melts from metasedimentary protoliths, i.e. 4.27 wt% in the CMT nanogranitoids

318 versus 0.9-3.9 wt% of the experimental dataset when taken on anhydrous basis, as compiled by

319 Stevens et al. (2007). The database of nanogranitoids and melt inclusions (Bartoli et al., 2016)

320 shows that most of the melt inclusions (for a total of ~600 analyses in 2016) show a

321 FeO+MgO+TiO_2 content in the range 0.25-2.50 wt%, with only ~10% of the whole database

322 having contents 4 - 5 wt%. As CMT nanogranitoids show an average FeO+MgO+TiO_2 =4.63

323 wt% (Table 2), their mafic component is higher than almost 90% of the anatectic melt inclusions

324 measured so far.

325   Experimental work on Fe and Mg contents in haplogranitic melts (Johannes and Holtz, 1996)

326 and melting experiments on metasediments (Patiño-Douce and Johnston, 1991; Montel and

327 Vielzeuf, 1997; Droop et al., 2003) show that a granitic melt produced during melting of

328 metasediments can accommodate a progressively higher amount of Fe and Mg as the formation T

329 of the melt increases. Such observations, so far rooted exclusively in experimental findings, are

330 now supported by our natural data. This is clearly visible when they are plotted against data

331 available in literature on granitic inclusions from metasediments melted at different T (Fig. 7; see

332 also Table 2). Different case studies of nanogranitoids show a positive correlation between

333 melting T (corresponding in turn to melt entrapment in the growing host) and FeO+MgO content.

334 Indeed, the melt in the CMT nanogranitoids, which shows the highest FeO+MgO content among

335 all the granitic inclusions, formed at $T \geq$ 1000°C, the highest formation T identified so far in

15

336 nanogranitoids from metasediments. Conversely, the melt produced at lower T, 700-710°C,

337 shows the lowest FeO+MgO content, in the range 1.34-1.83 wt%.

338 A variable degree of FeO+MgO enrichment is commonly observed in S-type (anatexis-related)

339 granites (e.g. Stevens et al., 2007; Villaros et al., 2009) and in leucosomes and small granite

340 sheets associated with migmatite bodies with sedimentary protoliths, coupled to increases in

341 A/CNK and decreases in silica content (Taylor and Stevens, 2012).This has been proposed to be

342 the result of selective entrainment in the magma of peritectic garnet, possibly the most common

343 repository of Fe, Mg and Al in metamorphosed crustal rocks, as the melt progressively coalesces

344 at depth and migrates upwards (Stevens et al., 2007). This hypothesis assumes that most pristine

345 anatectic melts from metasediments are leucogranitic and very low in mafic components, a

346 concept so far supported by both experiments (Stevens et al., 2007) and melt inclusions (Bartoli

347 et al., 2016). However, our study proves that anatectic melts can instead show a rather high

348 content of Fe and Mg when produced at T>1000°C and, thus, they should be considered to have a

349 pristine, "starting" composition (Ferrero et al., 2012; Bartoli et al., 2016). This observation does

350 not affect the validity of the peritectic phase entrainment hypothesis, which remains a sound

351 explanation for FeO+MgO enrichment in S-type granites. It does however pose a significant

352 caveat for researchers who want to correctly estimate the magnitude of peritectic phase

353 entrainment experienced by the granitic body/leucosome under investigation, warning in

354 particular against overestimating the magnitude of entrainment by assuming a too small

355 FeO+MgO content in the original anatectic melt when the latter is produced at T in excess of

356 950-1000 °C.

357

358 **Volatiles in high pressure melt**

359   H_2O is necessary to stabilize any silicate melt under crustal conditions, and the quantification of

360   H_2O, as well as of other species such as CO_2 and halogens, partitioned into deep partial melts is

361   of utmost importance for quantifying volatile cycles at depth and how they affect deep melting

362   processes (Bartoli et al., 2014). NanoSIMS analyses on re-homogenized nanogranitoids is a

363   routine approach in nanogranitoid studies (e.g. Acosta-Vigil et al. 2016), and it has shown that

364   nanogranitoids generally preserve their original composition in terms of H_2O (Bartoli et al., 2014)

365   and CO_2 contents (Carvalho et al., 2019). In particular, the loss of H_2O (even as OH) from the

366   inclusion to the matrix surrounding the garnet would shift the liquidus of the trapped melt toward

367   higher T (Johannes and Holtz, 1996). Thus the nanogranitoids would re-homogenize only at *T*

368   significantly higher than those obtained via independent geothermobarometry on the host rocks,

369   which is not the case here: the inclusions re-homogenize indeed at ~1050°C, consistently with the

370   *T* range of Zr-in-Rt thermometers on the rutile needles present in the nanogranitoid-bearing

371   garnets (Axler and Ague, 2015). In this work, the average H_2O value (4.40 wt%) is rather close to

372   that obtained via difference from 100 of the EMP totals after alkali loss correction (4.63 wt%).

373   Both values are consistent with experimental estimates of H_2O content in haplogranitic melts at

374   the PT conditions of interest, as the experimental parameters of the two successful experiments

375   (point 3 and 4 in Fig. 2) are close to the 4 wt% H_2O liquidus curve extrapolated at P >1.0 GPa

376   (Johannes and Holtz, 1996).

377   The melt also contains significant amounts of CO_2, on average ~ 3000 ppm (0.3 wt%). This

378   CO_2 may be internally produced as result of the devolatilization of hydrous silicates in the

379   presence of graphite (Connolly and Cesare, 1993; Cesare et al., 2005) visible in the CMT felsic

380   granulites as trapped minerals in inclusions and/or as mineral inclusions in garnet and the rock

381   matrix (Axler and Ague 2015). The CO_2 content of the CMT nanogranitoids is higher, on

17

382   average, than in the nanogranitoids measured in the graphite-bearing metasediments of the Ivrea-

383   Verbano Zone (IVZ; Carvalho et al., 2019), the only other case study so far where CO_2 was

384   measured in situ in re-homogenized nanogranitoids. It is likely that the different depth at which

385   melting occurred played a major role in shaping the CO_2 content of the melt. Experimental

386   studies have shown that CO_2 solubility in melt increases dramatically with increasing P (~500

387   ppm each 0.1 GPa in experimental studies; Ni and Keppler, 2013), and in fact our results show

388   that CMT nanogranitoids likely formed at significantly greater depth than IVZ nanogranitoids,

389   1.7-2.0 GPa (this study) vs. 0.8 GPa (Carvalho et al., 2019).

390   Probably the most striking feature of the CMT melt is the presence of a significant amount of

391   halogens. Chlorine (0.32 wt% average) and F (3161 ppm, or ~0.32 wt%) account together for

392   0.64 wt% on average of the total melt composition. This is also consistent with the fact that

393   phlogopite crystallized inside the CMT nanogranitoids has been found, in one case, to contain an

394   unusually high amount of F (>1 wt%; Axler and Ague, 2015). Halogens are characteristic of

395   brines, i.e. saline and Cl-rich fluid with low H_2O activity, proposed by some authors to play an

396   important role in the melting processes occurring in a thickened crust at either lower crustal or

397   upper mantle conditions (Aranovich et al., 2014). The Cl content of partial melts can be used as

398   proxy for the presence of brines during melt production at depth (Acosta-Vigil et al., 2016). CMT

399   nanogranitoids contain 0.10-0.98 wt% of Cl, an amount comparable to those reported in

400   experimental melts coexisting with brines, i.e., ranging between ~0.2 and 1.6 wt% (Webster and

401   Mandeville, 2007; Aranovich et al., 2013; Safonov et al., 2014). Experiments show furthermore

402   that brines in a haplogranitic system may cause a significant shift of the minimum melting T

403   toward higher values due to the lowering of the H_2O activity (Aranovich et al., 2013), thus

404   helping to create the conditions for melting to occur at extreme temperatures (>1000°C) as

18

405 proposed for the CMT felsic granulites, a notion independently supported by both previous PT

406 estimates (Ague et al., 2013; Axler and Ague, 2015) as well as by the complete re-

407 homogenization of the nanogranitoids at 1050°C. Another possibility is that the enrichment in

408 halogens predated the metamorphic peak, i.e. the brines were not present during melting but had

409 infiltrated the felsic granulites during their prograde metamorphic evolution. In this scenario, Cl

410 and F are incorporated in the biotite, and this process extends biotite stability field toward UHT

411 conditions (Martin and Hand, 2015), thus allowing biotite to destabilize at significantly higher *T*

412 than commonly expected.

413   **IMPLICATIONS and CONCLUSIONS**

414   The deep nature of granulite metamorphism and the high thermal flux required to achieve

415 melting favor post-melting re-equilibration and re-crystallization of granulites/migmatites, often

416 obliterating the most direct evidence of the presence of melt, such as leucosomes and melt

417 pseudomorphs (White et al., 2011). For this reason the preserved melt inclusions sheltered in

418 peak peritectic garnet of the CMT felsic granulites are a crucial finding. They indeed provide new

419 data necessary to a more comprehensive portrait of the multiple aspects of melting, melt

420 preservation, and crustal evolution during metamorphism in the deep roots of orogens. In

421 particular:

422   • HP melts from metasediments are still underrepresented in the nanogranitoid database, as

423 the bulk of the reported case studies of nanogranitoids are from rocks melted at P <1.5 GPa (see

424 lists in Cesare et al., 2015; Bartoli et al., 2016; Acosta-Vigil et al., 2016; Ferrero et al. 2018b).

425 The only two case studies of melts produced at P>1.5 GPa are from significantly greater depths

426 of 2.7 GPa (Ferrero et al. 2015) and >4.5 GPa (Stepanov et al 2016). Along with the recent work

427 on the metasomatic nanogranitoids hosted in the Granulitgebirge pyroxenites (Borghini et al.,

428   2018; 2020), our data are a step toward filling the gap in knowledge on natural partial melts

429   forming at intermediate P (~2.0 GPa). A further important feature of CMT nanogranitoids is the

430   fact that they are richer in mafic components (FeO and MgO) than the majority of nanogranitoid

431   case studies. Their pristine nature thus provides a direct confirmation that the granitic melt from

432   anatexis can accommodate an increasing amount of Fe and Mg with increasing T, an observation

433   rooted until now exclusively in experimental studies. This finding is thus a caveat against

434   assuming that natural pristine anatectic melts are always leucogranitic.

435   • Our independent experimental results provide the first evidence of HP conditions during

436   the metamorphic peak / melting of the felsic granulites in the Central Maine Terrane, pointing

437   toward melting conditions of ~1050°C and 1.7-2.0 GP. HP metamorphism, rather than purely

438   UHT (Ague et al., 2013), is also supported by the widespread presence of pseudomorphs of

439   sillimanite after kyanite in the matrix (Axler and Ague, 2015). Our findings warrants a

440   reappraisal of the metamorphic peak conditions in the area and finds direct support in other recent

441   studies in nearby localities: HP conditions (1.8 GPa) reported in silica-undersaturated gneisses

442   (Keller and Ague, 2018), whereas other metapelites contain evidence of UHP metamorphism (>5

443   GPa; Keller and Ague, 2020);

444   • H_2O, CO_2, Cl and F were measured directly in situ in the HP crustal melt still preserved in

445   its original source rock. H_2O was so far measured in nanogranitoids from rocks equilibrated

446   between ~0.4 GPa and 1.4 GPa (Bartoli et al., 2014; 2016; Acosta-Vigil et al., 2016; Carvalho et

447   al., 2019), whereas CO_2 in situ measurements are only available from the IVZ, equilibrated at 0.8

448   GPa (Carvalho et al. 2019). Our new measurements extend the existent dataset toward

449   significantly greater depth and provide the foundation of further studies to further clarify how the

450   interplay of protolith, fluid speciation, and PT conditions influence H_2O and carbon budgets

451   during crustal subduction and thickening. Moreover, to our knowledge our study presents the first

452   data on F measured in situ in anatectic melt inclusions. Previous experimental studies suggest that

453   the presence of a significant amount of Cl such as the one measured in the CMT inclusions may

454   be indicative of the presence of saline fluids, e.g. brine, during melting. This is the first direct

455   natural evidence that brines infiltrating the lower crust as a metasomatic fluid may be an

456   influential factor for the establishment of conditions necessary to produce melt at such extreme

457   temperatures (>1000°C), commonly inferred to be characterized by fluid-absent melting

458   conditions.

459

469

470   *References*

471   Acosta-Vigil, A., Barich, A., Bartoli, O., Garrido, C.J., Cesare, B., Remusat, L., Poli, S.,
472   andRaepsaet, C. (2016). The composition of nanogranitoids in migmatites overlying the Ronda
473   peridotites (Betic Cordillera, S Spain): the anatectic history of a polymetamorphic basement.
474   Contributions to Mineralogy and Petrology, 171, 24.

Acosta-Vigil, A., Cesare, B., London, D., Morgan, G. B., VI (2007). Microstructures and composition of melt inclusions in a crustal anatectic environment, represented by metapelitic enclaves within El Hoyazo dacites, SE Spain. Chemical Geology 235, 450-465.

Aranovich, L.Y., Makhluf, A.R., Manning, C.E., and Newton, R.C. (2014) Dehydration melting and the relationship between granites and granulites. Precambrian Research, 253, 26–37.

Aranovich, L.Y., Newton, R.C., and Manning, C.E. (2013) Brine-assisted anatexis: experimental melting in the system haplogranite–H_2O–NaCl–KCl at deep-crustal conditions. Earth and Planetary Science Letters 374, 111-120.

Auzanneau, E., Vielzeuf, D., and Schmidt, M.W. (2006) Experimental evidence of decompression melting during exhumation of subducted continental crust. Contributions to Mineralogy and Petrology, 152, 125–148.

Axler, J.A., and Ague, J.J. (2015) Oriented multiphase needles in garnet from ultrahigh-temperature granulites. American Mineralogist, 100, 2254–2271.

Bartoli, O., Acosta-Vigil, A., Ferrero, S., and Cesare, B. (2016) Granitoid magmas preserved as melt inclusions in high-grade metamorphic rocks. American Mineralogist, 101, 1543–1559.

Bartoli, O., Cesare, B., Poli, S., Acosta-Vigil, A., Esposito, R., Turina, A., Bodnar, R.J., Angel, R.J., and Hunter, J. (2013a) Nanogranite inclusions in migmatitic garnet: Behavior during piston cylinder re-melting experiments. Geofluids, 13, 405–420.

Bartoli, O., Cesare, B., Poli, S., Bodnar, R.J., Acosta-Vigil, A., Frezzotti, M.L., and Meli, S. (2013b) Recovering the composition of melt and the fluid regime at the onset of crustal anatexis and S-type granite formation. Geology, 41, 115–118.

Bartoli, O., Cesare, B., Remusat, L., Acosta-Vigil, A. and Poli, S. (2014) The H2O content of granite embryos. Earth and Planetary Science Letters 395, 281-290.

Bodnar RJ (2003) Reequilibration of fluid inclusions. In I. Samson, A. Anderson, & D. Marshall, eds. Fluid Inclusions: Analysis and Interpretation. Mineral. Assoc. Canada, Short Course 32, 213-230.

Borghini, A., Ferrero, S., Wunder, B., Laurent, O., O'Brien, P. J., and Ziemann, M. A. (2018) Granitoid melt inclusions in orogenic peridotite and the origin of garnet clinopyroxenite. Geology, 46(11), 1007–1010.

Borghini, A., Ferrero, S., O'Brien, P. J., Laurent, O., Günter, C., and Ziemann, M. A. (2020) Cryptic metasomatic agent measured in situ in Variscan mantle rocks: Melt inclusions in garnet of eclogite, Granulitgebirge, Germany. Journal of Metamorphic Geology, 38, 207–234.

Brown, M., 2006. Duality of thermal regimes is the distinctive characteristic of plate tectonics since the Neoarchean. Geology, 34, 961e964.

Bureau, H., Trocellier, P., Shaw, C., Khodja, H., Bolfan-Casanova, N., Demouchy, S., 2003. Determination of the concentration of water dissolved in glasses and minerals using nuclear microprobe. Nucl. Instrum. Methods Phys. Res., Sect. B 210, 449–454.

Carvalho, B. B., Bartoli, O., Ferri, F., Cesare, B., Ferrero, S., Remusat, L., Capizzi, L.S., Poli, S. (2019). Anatexis and fluid regime of the deep continental crust: New clues from melt and fluid inclusions in metapelitic migmatites from ivrea zone (NW italy). Journal of Metamorphic Geology, 37, 951-975. 63

Connolly, J. A. D. And Cesare, B. (1993) C-O-H-S fluid composition and oxygen fugacity in graphitic metapelites. Journal of Metamorphic Geology, 11, 368-378.

Cesare, B., Acosta-Vigil, A., Bartoli, O., and Ferrero, S. (2015) What can we learn from melt inclusions in migmatites and granulites? Lithos, 239, 186–216.

520   Cesare, B., Meli, S., Nodari, L., and Russo, U., (2005) Fe^{3+} reduction during biotite melting in
521   graphitic metapelites: another origin of CO_2 in granulites. Contributions to Mineralogy and
522   Petrology, 149, 129–140.
523   Cesare, B., Ferrero, S., Salvioli-Mariani, E., Pedron, D., and Cavallo, A. (2009a) Nanogranite
524   and glassy inclusions: the anatectic melt in migmatites and granulites. Geology, 37, 627–630.
525   Créon, L., Levresse, G., Remusat, L., Bureau, H. and Carrasco-Núñez, G. (2018) New method
526   for initial composition determination of crystallized silicate melt inclusions. Chemical Geology
527   483, 162-173.
528   Darling, R. S., Chou, I.-M., and Bodnar, R. J. (1997) An occurrence of metastable cristobalite
529   in high-pressure garnet granulite. Science, 276, 91–93.
530   Droop, G.T.R., Clemens, J.D., and Dalrymple, J. (2003) Processes and conditions during
531   contact anatexis, melts escape and restite formation: The Huntly Gabbro complex, NE Scotland.
532   Journal of Petrology, 44, 995–1029.
533   Ferrero, S., and Angel, R. J. (2018) Micropetrology: are inclusions in minerals grains of truth?
534   Journal of Petrology, 59, 1671–1700.
535   Ferrero, S., Bodnar, R.J., Cesare, B., and Viti, C. (2011) Reequilibration of primary fluid
536   inclusions in peritectic garnet from metapelitic enclaves, El Hoyazo, Spain. Lithos, 124, 117–
537   131.
538   Ferrero, S., Bartoli, O., Cesare, B., Salvioli-Mariani, E., Acosta-Vigil, A., Cavallo, A., Groppo,
539   C., and Battiston, S. (2012) Microstructures of melt inclusions in anatectic metasedimentary
540   rocks. Journal of Metamorphic Geology, 30, 303–322.
541   Ferrero, S., Wunder, B., Ziemann, Wälle, M., and O'Brien, P.J. (2016a) Carbonatitic and
542   granitic melts produced under conditions of primary immiscibility during anatexis in the lower
543   crust. Earth Planetary Science Letters, 454, 121–131.
544   Ferrero, S., Ziemann, M.A., Angel, R.J., O'Brien, P.J. and Wunder, P.J. (2016b) Kumdykolite,
545   kokchetavite, and cristobalite crystallized in nanogranites from felsic granulites, Orlica Snieznik
546   Dome (Bohemian Massif): not evidence for ultrahigh pressure conditions. Contributions to
547   Mineralogy and Petrology, 171, 3.
548   Ferrero, S., Godard, G., Palmeri, R., Wunder, B., and Cesare B. (2018a) Partial melting of
549   ultramafic granulites from Dronning Maud Land, Antarctica: Constraints from melt inclusions
550   and thermodynamic modelling. American Mineralogist, 103, 610-622.
551   Ferrero, S., O'Brien, P. J., Borghini, A., Wunder, B., Wälle, M., Günter, C., and Ziemann, M.
552   A. (2018b) A treasure chest full of nanogranitoids: an archive to investigate crustal melting in the
553   Bohemian Massif, in Ferrero, S., Lanari, P., Goncalves, P., and Grosch, E. G., eds., Metamorphic
554   Geology: Microscale to Mountain Belts: Geological Society, London, Special Publications 478,
555   13-38.
556   Ferrero S, Wunder B, Walczak K, Ziemann MA, O'Brien PJ (2015). Preserved near ultrahigh-
557   pressure melt from continental crust subducted to mantle depths. Geology, 43, 447-450.
558   Hauri, E., Wang, J., Dixon, J.E., King, P.L., Mandeville, C. and Newman, S. (2002) SIMS
559   analysis of volatiles in silicate glasses: 1. Calibration, matrix effects and comparisons with FTIR.
560   Chemical Geology 183, 99-114.
561   Hwang, S-L., Shen, P., Chu, H-T., Yui, T-F, Liou, J-G., Sobolev, N.V., Zhang, R.Y., Shatsky,
562   V.S., and Zayachkovsky, A.A. (2004) Kokchetavite: a new polymorph of $KAlSi_3O_8$ from the
563   Kokchetav UHP terrain. Contributions to Mineralogy and Petrology, 148: 380–389.
564   Johannes, W., and Holtz, F. (1996) Petrogenesis and experimental petrology of granitic rocks,
565   335 p. Berlin, Springer.
23

566   Le Breton, N., and Thompson, A.B. (1988) Fluid-absent (dehydration) melting of biotite in
567   metapelites in the early stages of crustal anatexis. Contributions to Mineralogy and Petrology, 99,
568   226–237.
569   Morgan G.B.VI, and London, D. (2005a) Effect of current density on the electron microprobe
570   analysis of alkali aluminosilicate glasses. American Mineralogist, 90, 1131–1138.
571   Montel, J.-M., and Vielzeuf, D. (1997). Partial melting of metagreywackes, Part II.
572   Compositions of minerals and melts. Contributions to Mineralogy and Petrology, 128, 176–196.
573   Ni, H., and Keppler, H. (2013). Carbon in silicate melts. Reviews in Mineralogy &
574   Geochemistry, 75, 251-287.
575   O'Brien, P.J., and Ziemann, M.A. (2008) Preservation of coesite in exhumed eclogite: insights
576   from Raman mapping. European Journal of Mineralogy, 20, 827-834.
577   Patiño Douce, A.E., and Johnston, A.D. (1991) Phase equilibria and melt productivity in the
578   pelitic system: implications for the origin of peraluminous granitoids and aluminous granulites.
579   Contributions to Mineralogy and Petrology 107, 202–218.
580   Safonov, O.G., Kosova, S.A., and van Reenen, D.D. (2014) Interaction of biotite-amphibole
581   gneiss with H_2O–CO_2–(K, Na)Cl fluids at 550 MPa and 750 and 800 °C: experimental study and
582   applications to dehydration and partial melting in the middle crust. Journal of Petrology, 55,
583   2419–2456.
584   Stepanov, A.S., Hermann, J., Rubatto, D., Korsakov, A.V., Danyushevsky, L.V. (2016) Melting
585   History of an Ultrahigh-pressure Paragneiss Revealed by Multiphase Solid Inclusions in Garnet,
586   Kokchetav Massif, Kazakhstan. Journal of Petrology, 57, 1531-1554.
587   Stevens, G., Villaros, A., and Moyen, J.-F. (2007) Selective peritectic garnet entrainment as the
588   origin of geochemical diversity in S-type granites. Geology 35, 9–12.
589   Taylor, J., and Stevens, G. (2010). Selective entrainment of peritectic garnet into S-type
590   granitic
591   magmas: evidence from Archaean mid-crustal anatectites. Lithos, 120, 277–292.
592   Thomen, A., Robert, F. and Remusat, L. (2014) Determination of the nitrogen abundance in
593   organic materials by NanoSIMS quantitative imaging. Journal of Analytical Atomic
594   Spectrometry 29, 512-519.
595   Villaros, A., Stevens, G., Moyen, J.F., and Buick, I.S. (2009). The trace element compositions
596   of S-type granites: evidence for disequilibrium melting and accessory phase entrainment in the
597   source. Contributions to Mineralogy and Petrology, 158, 543–561.
598   Webster, J.D., and Mandeville, C.W. (2007) Fluid immiscibility in volcanic environments. In:
599   Liebscher A, Heinrich CA (eds) Fluid-fluid interactions. Reviews in Mineralogy and
600   Geochemistry, 65, 313–362.
601   White, R.W., Stevens, G., and Johnson, T.E. (2011) Is the crucible reproducible? Reconciling
602   melting experiments with thermodynamic calculations. Elements, 7, 241–246.
603   Whitney, D.L., and Evans, B.W. (2010) Abbreviations for names of rock-forming minerals.
604   American Mineralogist, 95, 185–187.
605

606
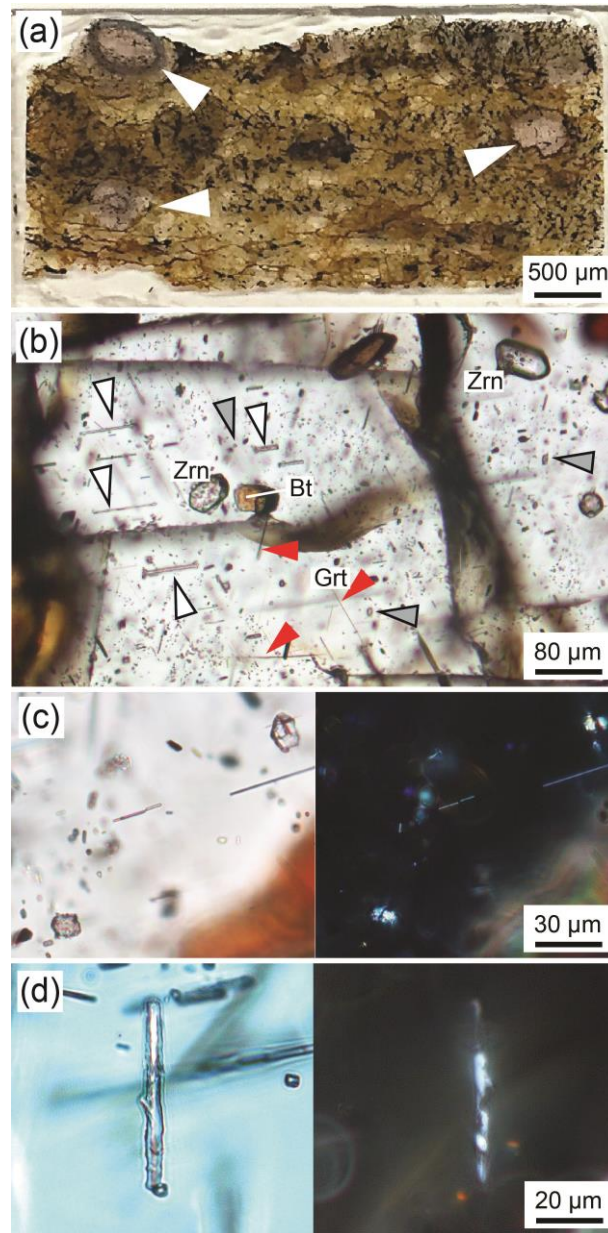
FIGURE 1. A) Microstructural features of inclusions and host rocks. (**a**) Scan of a representative thin section with garnets in a more felsic matrix; the garnet in the upper left corner has a circle made with a black marker. *White arrows:* MI-bearing garnets. (**b**) Cluster of polycrystalline inclusions occurring in the center of the garnet, mineral abbreviations from Whitney and Evans (2010). *White arrows:* needle shaped nanogranitoids. Gray arrows: isometric nanogranitoids, generally smaller than the first inclusion type. *Red arrows:* thin rutile needles. (**c**)

613　Close up of isometric nanogranitoids (**left**) with multiple birefringent phases visible under

614　crossed polars (**right**). (**d**) Close up of a needle shaped nanogranitoid (**left**), occasionally with the

615　rough outline already described by Axler and Ague (2015), and showing once again several

616　birefringent phases under crossed polars (**right**).

617

618

619
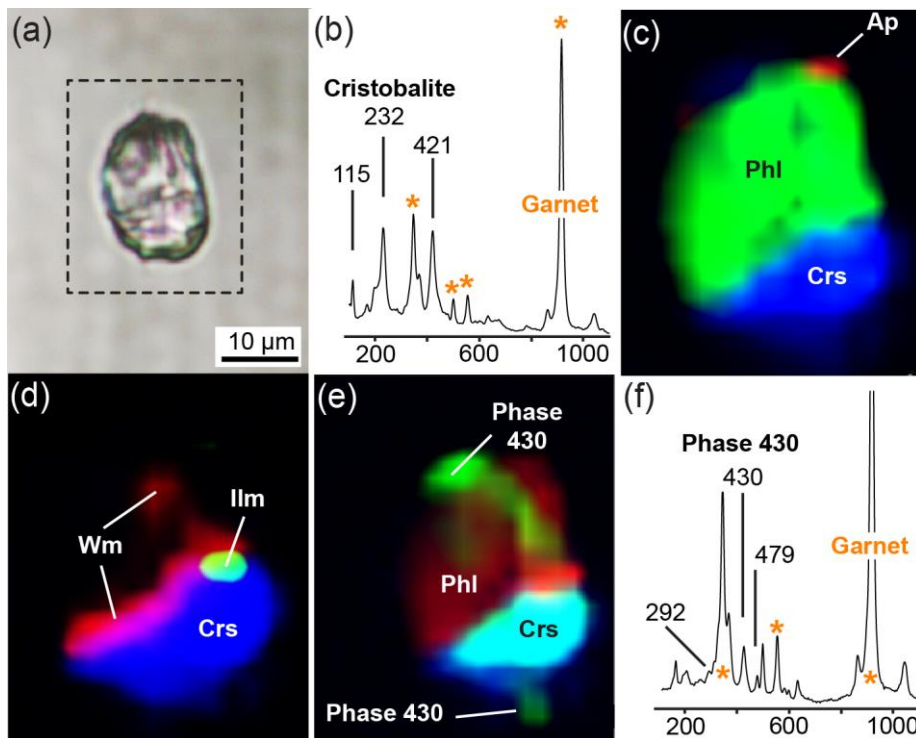
620

621　　FIGURE 2. Results of MicroRaman investigation of a representative inclusion below the

622　surface (**a**). (**b**) Raman spectrum of cristobalite from the CMT nanogranitoids. (**c**) The map

623　shows the distribution of Raman peak 415 cm^{-1} of cristobalite (blue), 196 cm^{-1} of phlogopite

624　(green) and 963 cm^{-1} of apatite (red). In (**d**) also the distribution of peak 707 of white mica (red)

625　and the 675 cm^{-1} peak of ilmenite (green) are visible. In (e) the distribution of peak 430 cm^{-1} is

626　visible in green, whereas in (f) a representative spectrum of phase 430 is reported.

627
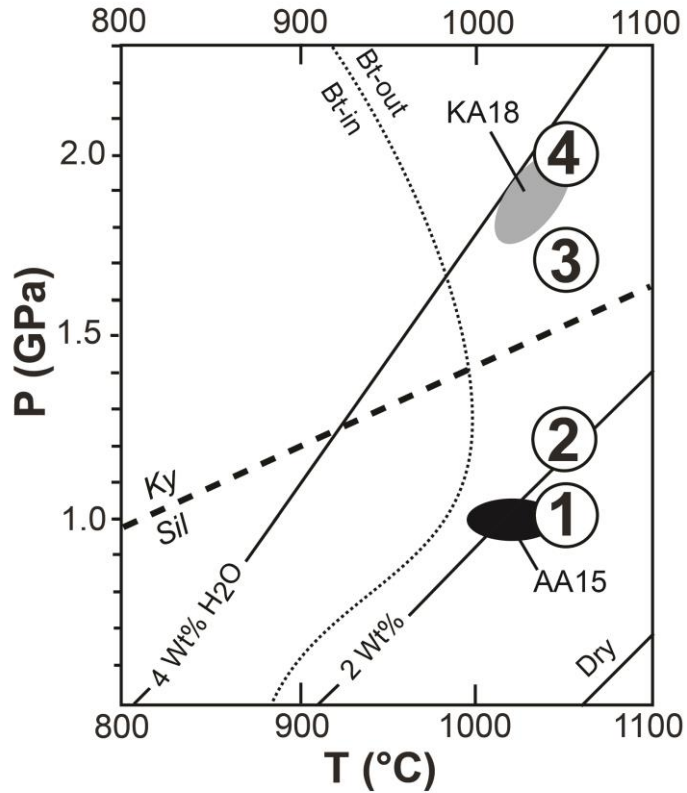
FIGURE 3: Experimental conditions (numbers in circles) versus previous estimates of metamorphic peak equilibration for the host gneisses of the investigated nanogranitoids. Solid lines: liquidus curves for different amount of H_2O according to Johannes and Holtz (1996). AA15: Temperature and minimum P conditions proposed by Axler and Ague (2015) for the felsic granulites investigated in the present study. KA18: HP conditions estimated on garnet-spinel-corundum gneisses of the Central Maine Terrane by Keller and Ague (2018).

634

635
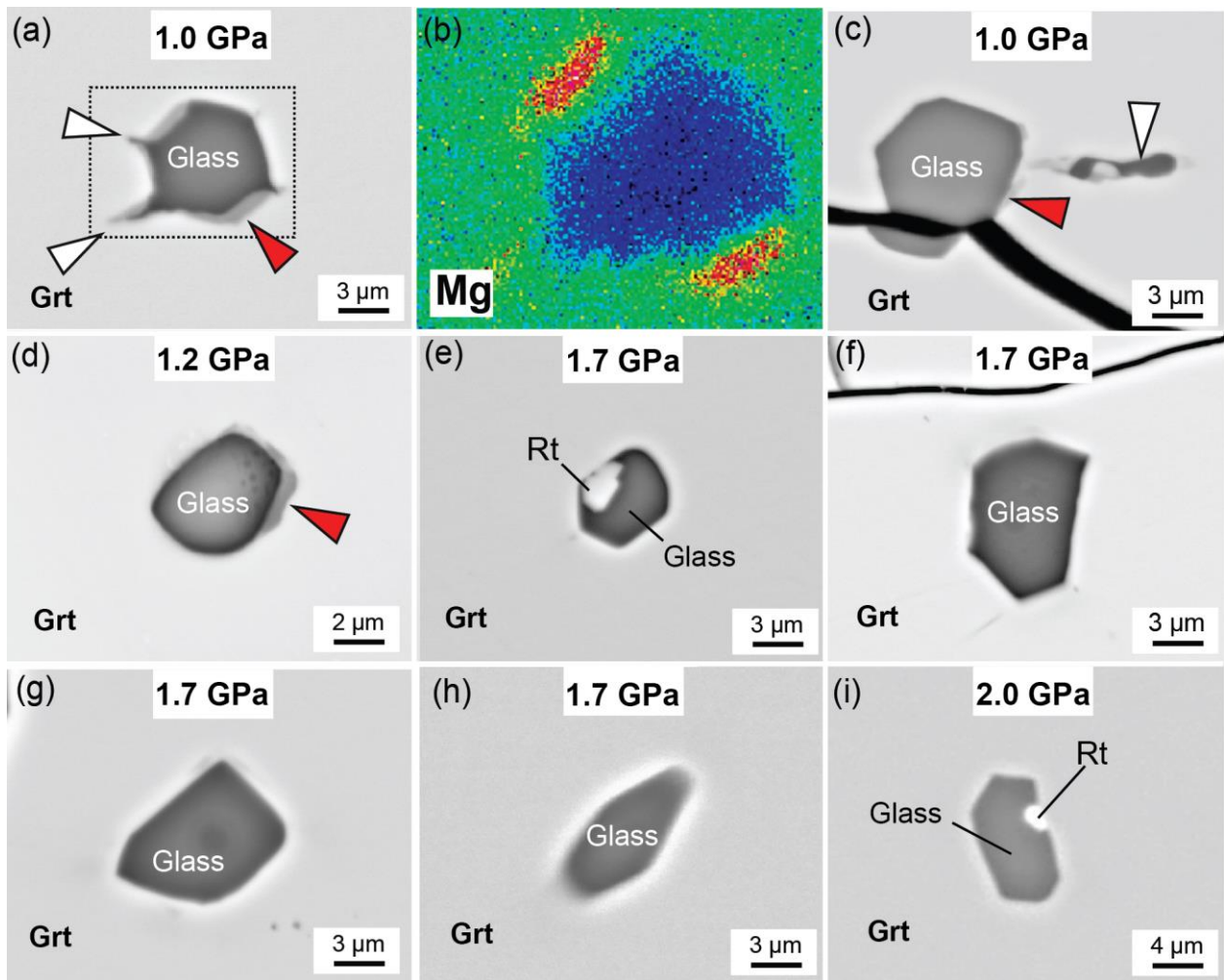
FIGURE 4. BSE images of CMT nanogranitoids after piston cylinder experiments under different confining *P*. *White arrows:* decrepitation cracks. *Red arrows*: new Mg-richer garnet. See text for details on the single images.

641
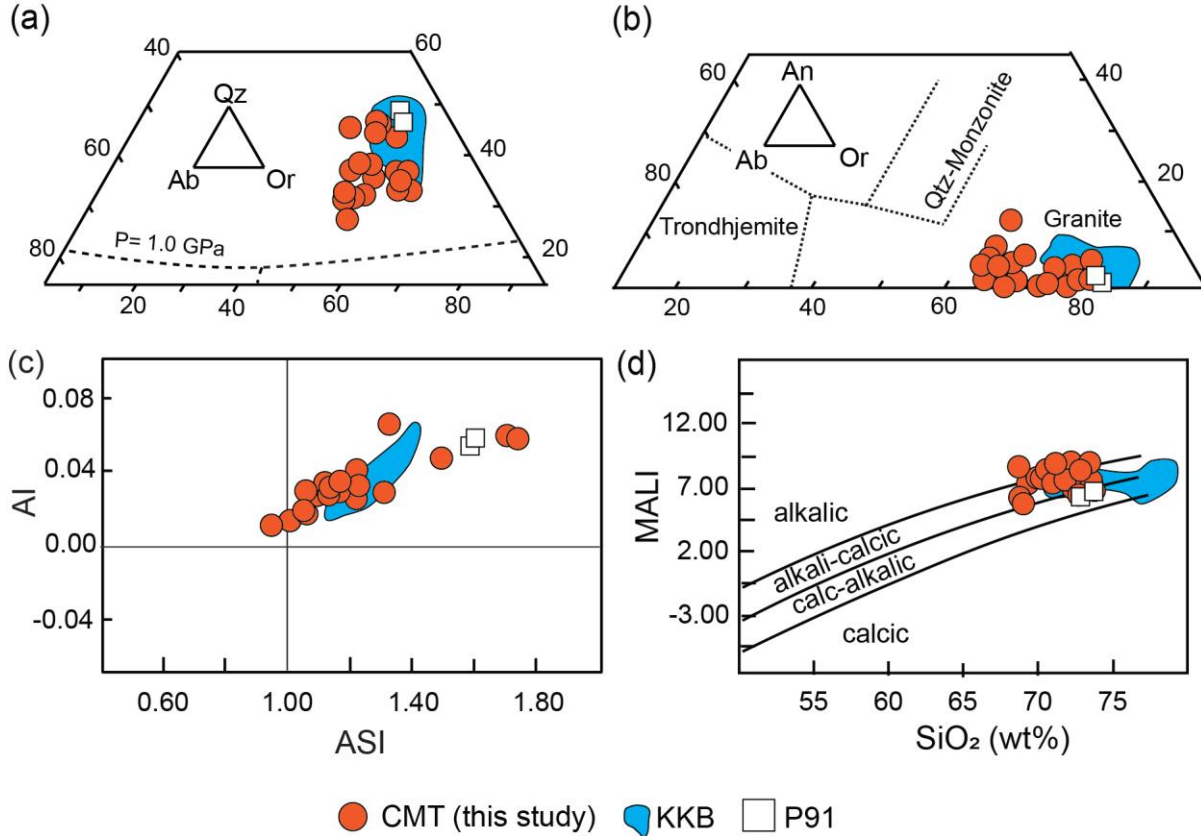
644　　　FIGURE 5: composition of re-homogenized nanogranitoids. (**a**) Ab-Or-Qz and (**b**) Ab-Or-An

645　　normative diagrams. (**c**) Alumina Saturation Index (ASI)= molar Al/(Ca+Na+K)) versus

646　　Alkalinity Index (AI)= molar Al-(Na+K). (**d**) Silica content versus Modified Alkali-Lime Index

647　　(MALI)= Na_2O+K_2O-CaO. CMT= central Maine Terrane; KKB= UHT nanogranites of the

648　　Kerala Khondalite Belt (Ferrero et al., 2012). P91= experimental melts from Patiño-Douce and

649　　Johnston (1991). For EMP compositions and *P-T* conditions of formation of the KKB and P91

650　　melts see Table 2.

(a)

Glass, **Garnet**

H$_2$O in glass

500   1500   2500   3500
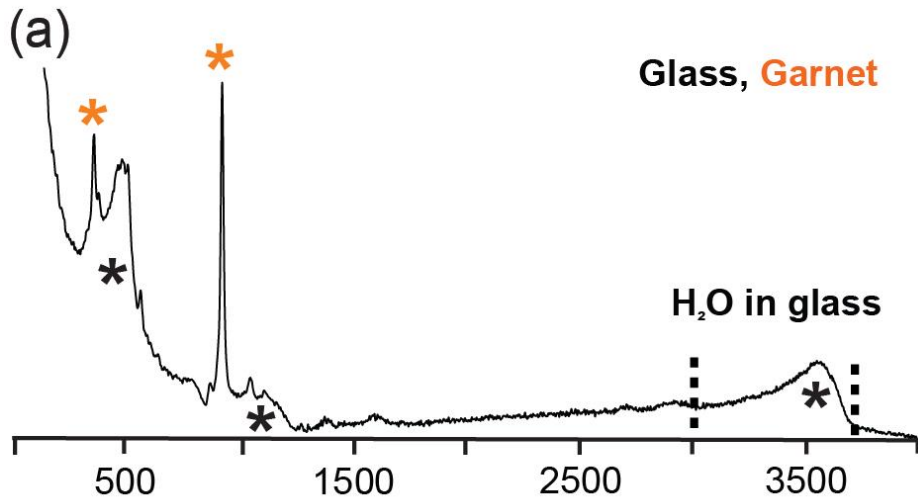
651

652   FIGURE 6: Raman spectrum of nanogranitoid re-homogenized to glass.

653
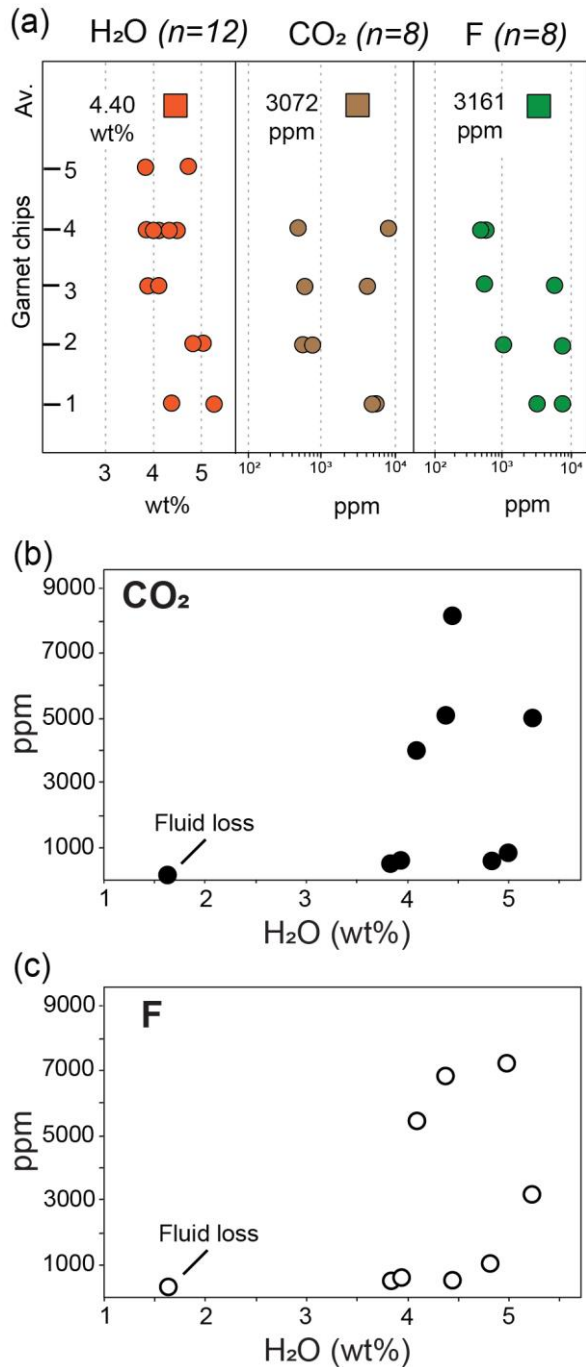
FIGURE 7: NanoSIMS measurements on re-homogenized nanogranitoids. (**a**) Measurements of H_2O, CO_2 and F presented according to the garnet chip in which they were measured. Variation diagrams of (**b**) CO_2 and (c) F with respect to H_2O for each single NanoSIMS analysis, including one inclusion with clear fluid loss (indicated in figure).

659
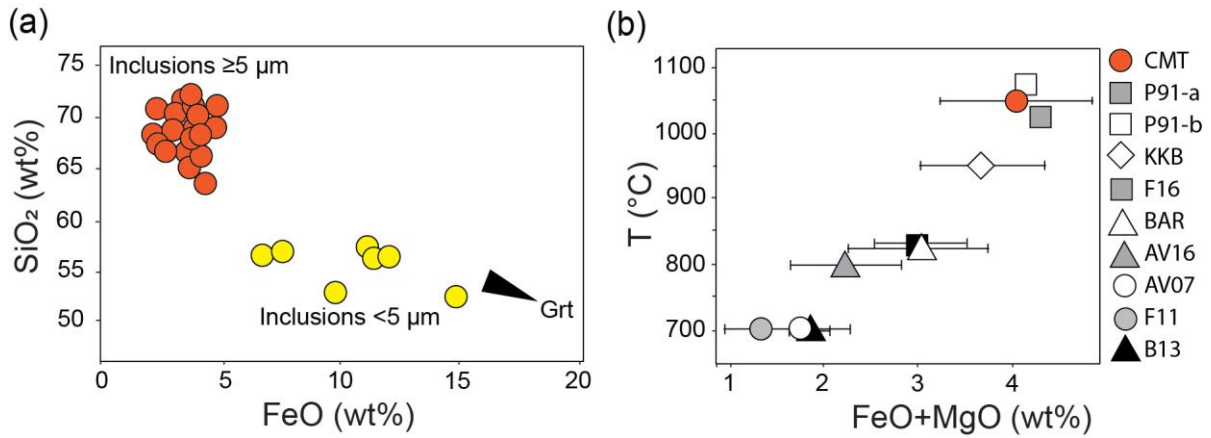
FIGURE 8. High FeO+MgO content in re-homogenized CMT nanogranitoids. (**a**) Comparison between inclusion with diameter ≥5 µm (orange circles) and <5 µm (yellow circles). (**b**) FeO+MgO versus T diagram, comparing nanogranitoids compositions from this study with previous case studies of inclusions in partially melted rocks with metasedimentary protolith (including standard deviations; data from Table 2). For abbreviations see caption Table 2.

665

Experiment	Figures	T(°C)	P (GPa)	t (h)	Melting	Decrepitation	Melt-host interaction	Full Re-homogenization
1	Fig. 4a,b,c	1050	1.0	≈15	X	X (extensive)	X (new Grt+New Opx)	-
2	Fig. 4d	1050	1.2	24	X	-	X (new Grt)	-
3	Fig. 4e,f,g,h	1050	1.7	24	X	-	-	X
4	Fig. 4i	1050	2.0	24	X	-	-	X

666

667   Table 1: Conditions, relevant info and results of piston cylinder experiments.

33

	Central Maine Terrane																					Experiments			Other Nanogranitoids					
n=19	21	43	av.44-4	18	20	21	22	23	24	7	8	32	35	34	3	6	36	39	21/22	Aver.	Stdv	P91	P91	KKB	BAR	F16	AV16	AV07	F11	B13
n=																								n=11	n=4	n=4	n=5	n=62	n=15	n=15
Duration	24h	24h	24h	24h	24h	24h	24h	24h	24h	24h	24h	24h	24h	24h	24h	24h	24h	24h	4h											
T (°C)	1050	1050	1050	1050	1050	1050	1050	1050	1050	1050	1050	1050	1050	1050	1050	1050	1050	1050	1050			1025	1075	950	830	825	800	700	700	700
P (Gpa)	1.7	1.7	1.7	1.7	1.7	1.7	1.7	1.7	1.7	1.7	1.7	1.7	1.7	2.0	2.0	2.0	2.0	2.0	2.0			1.0	1.0	0.5	0.8	0.5	1.2/1.4	0.5	0.5	0.5
Wt%																														
SiO$_2$	64.96	68.89	63.61	67.10	69.15	68.22	67.64	66.00	68.32	66.80	67.30	70.97	70.92	68.83	71.07	68.24	71.97	71.91	66.36	**68.33**	(2.34)	70.62	69.44	73.96 (2.63)	73.77 (2.34)	70.78 (3.44)	70.16 (1.29)	71.23 (1.43)	68.95 (1.65)	70.03 (2.28)
TiO$_2$	0.64	0.36	0.03	0.05	0.91	0.24	0.14	0.14	0.10	0.05	0.16	0.22	0.15	0.13	0.10	0.00	0.33	0.66	0.07	**0.23**	(0.25)	0.65	0.73	0.11 (0.09)	0.09 (0.08)	0.06 (0.05)	0.07 (0.06)	0.10 (0.03)	0.10 (0.12)	0.04 (0.07)
Al$_2$O$_3$	12.61	12.50	14.74	12.39	12.96	12.89	13.80	12.42	13.71	12.84	14.03	13.18	14.00	12.06	11.83	13.46	13.23	11.93	13.14	**13.04**	(0.81)	13.4	13.64	12.95 (1.31)	12.90 (1.46)	11.91 (0.68)	14.89 (0.98)	14.44 (0.33)	12.82 (1.14)	11.71 (0.86)
FeO	3.71	4.76	4.43	3.27	3.22	3.53	3.25	4.10	3.08	2.89	2.38	3.53	2.41	3.97	4.75	2.22	3.49	3.47	3.54	**3.47**	(0.74)	3.26	3.04	3.03 (0.69)	2.51 (0.37)	2.39 (0.76)	2.14 (0.59)	1.71 (0.52)	1.32 (0.40)	1.71 (0.21)
MnO	0.11	0.11	0.04	0.02	0.09	0.14	0.02	0.08	0.01	0.00	0.00	0.06	0.09	0.01	0.00	0.03	0.08	0.08	0.07	**0.05**	(0.05)	0.11	0.08	0.04 (0.03)	0.25 (0.17)	0.10 (0.10)	0.46 (0.07)	0.08 (0.05)	0.16 (0.17)	0.17 (0.10)
MgO	0.61	0.58	0.63	1.11	0.38	0.41	0.70	1.01	0.63	0.57	0.30	0.62	0.45	0.56	0.61	0.34	0.52	0.54	1.18	**0.62**	(0.20)	1.04	1.09	0.65 (0.21)	0.53 (0.13)	0.61 (0.07)	0.09 (0.02)	0.05 (0.04)	0.02 (0.03)	0.12 (0.07)
CaO	1.17	0.98	1.68	0.01	0.36	0.14	0.12	0.36	0.03	0.94	0.55	1.09	0.58	0.54	0.60	0.98	0.56	0.84	0.88	**0.65**	(0.45)	0.26	0.28	0.53 (0.20)	0.85 (0.48)	1.04 (0.56)	0.48 (0.13)	0.60 (0.09)	0.68 (0.16)	0.45 (0.13)
Na$_2$O	1.32	1.28	1.58	1.71	1.28	1.50	1.66	1.17	1.14	1.89	1.68	2.11	2.17	2.29	2.45	3.03	2.68	0.96	1.52	**1.76**	(0.58)	0.79	0.84	1.10 (0.32)	1.94 (0.13)	0.57 (0.45)	2.88 (1.24)	3.63 (0.39)	2.25 (0.35)	2.79 (0.35)
K$_2$O	6.93	7.00	5.11	6.10	7.23	7.17	4.71	5.23	5.51	6.01	7.41	5.81	6.68	6.18	6.07	6.69	6.51	6.45	6.13	**6.26**	(0.78)	5.98	6.05	6.72 (0.70)	4.86 (0.79)	6.24 (1.10)	3.97 (1.00)	4.97 (0.31)	4.56 (0.83)	4.05 (0.39)
P$_2$O$_5$	0.59	0.75	0.28	0.05	0.18	0.15	0.16	0.12	0.07	0.23	0.19	0.17	0.07	0.07	0.00	0.12	0.25	0.20	0.38	**0.21**	(0.19)	0.11	0.06	0.03 (0.05)	0.02 (0.02)	0.28 (0.09)	0.01 (0.01)	0.37 (0.09)	0.16 (0.07)	0.26 (0.23)
Cl	0.07	0.21	0.08	0.86	0.82	0.68	0.95	0.93	0.97	0.01	0.04	0.00	0.01	0.09	0.10	0.10	0.10	0.00	0.01	**0.32**	(0.39)	-	-	-	-	-	-	-	-	-
Total	92.64	97.21	92.12	91.79	95.76	94.38	92.20	92.59	96.17	98.00	97.76	97.53	94.64	97.49	99.07	99.57	97.05	93.29		**95.37**		96.22	95.25	99.12	97.73	93.97	95.15	97.16	91.02	91.33
Q	26	30	27	29	31	29	36	34	37	32	30	31	29	27	27	25	27	37	29	**30**		39	37	37	39	39	35	29	36	36
C	2	3	4	3	3	3	6	4	6	2	2	2	2	1	0	0	1	2	3	**3**		5	5	3	3	3	5	3	3	3
Or	41	41	30	36	43	42	28	31	33	37	45	34	39	37	36	41	38	38	36	**37**		35	36	40	29	37	23	29	27	24
Ab	11	11	13	14	11	13	14	10	10	15	14	18	18	19	21	25	23	8	13	**15**		7	7	9	16	5	24	31	19	24
An	2	0	7	0	1	0	0	1	0	3	1	4	2	2	3	3	1	3	2	**2**		1	1	2	4	3	2	1	2	1
Hy	7	10	10	9	6	7	8	10	7	7	5	8	5	8	10	4	7	7	9	**7**		8	7	7	6	6	5	3	3	4
ASI	1.07	1.09	1.32	1.31	1.22	1.23	1.71	1.51	1.74	1.11	1.16	1.12	1.18	1.05	1.01	0.95	1.06	1.18	1.22	**1.22**		1.63	1.62	1.29	1.29	1.24	1.50	1.16	1.30	1.19
H$_2$O by diff	7.36	2.79	7.88	8.21	4.24	5.62	7.80	9.38	7.41	3.83	2.00	2.24	2.47	2.51	0.93	0.43	2.95	6.72		**4.63**		3.78	4.75	0.88	2.27	6.03	4.85	2.84	8.98	8.67
Mg#	0.22	0.18	0.20	0.38	0.17	0.16	0.27	0.30	0.27	0.26	0.18	0.24	0.24	0.20	0.19	0.21	0.21	0.21	0.37	**0.23**		0.35	0.38	0.27	0.26	0.30	0.06	0.04	0.03	0.10
FeO+MgO+TiO$_2$	4.95	5.69	5.08	4.42	4.51	4.17	4.09	5.24	3.80	3.51	2.84	4.36	3.02	4.66	5.46	2.56	4.34	4.67	4.79	**4.30**		4.95	4.86	3.79	3.13	3.05	2.30	1.86	1.44	1.87
FeO+MgO	4.31	5.34	5.05	4.37	3.60	3.94	3.95	5.11	3.70	3.47	2.67	4.15	2.86	4.53	5.36	2.56	4.01	4.01	4.72	**4.05**		3.94	3.92	3.68	3.04	2.99	2.23	1.76	1.34	1.83
K$_2$O/Na$_2$O	5.24	5.48	3.24	3.57	5.64	4.79	2.84	4.48	4.82	3.18	4.41	2.76	3.07	2.69	2.48	2.21	2.43	6.71	4.04	**3.89**		7.57	7.20	6.09	2.51	11.01	1.38	1.37	2.02	1.45

Table 2: Geochemistry and PT conditions of formation of re-homogenized melt inclusions from the Central Maine Terrane, high temperature experimental melts from metasediments (P91= Patiño-Douce and Johnston, 1991) and averages of melt inclusion analyses from different case studies of metasediments melted under different conditions. KKB (Kerala Khondalite Belt, Southern India) and BAR (Barun gneiss, Himalaya) are from Ferrero et al., (2012). F16 = Oberpfalz migmatites from Ferrero et al. (2016). AAV16= Jubrique migmatites, Betic Cordillera (S Spain) from Acosta-Vigil et al., (2016). AAV07= Grt+Bt granulitic enclaves of El Hoyazo, Neogene Volcanic Province (S Spain) from Acosta-Vigil et al., (2007). F11= Spl-Crd granulitic enclaves of El Hoyazo from Ferrero et al. (2011). B13= Sierra Alpujata metatexites, Betic Cordillera (S Spain) from Bartoli et al., (2013).

677

Garnet	Analysis	H_2O (wt.%)	1σ error	CO_2 (ppm)	*1σ error*	F (ppm)	*1σ error*
1	Exp4_M1_1	4.38	*0.05*	5073	*204*	6820	*106*
	Exp4_M4_1	5.24	*0.06*	4979	*201*	3198	*49*
2	Exp4_M2_1	4.83	*0.05*	538	*32*	1033	*15*
	Exp4_M3_1	5.00	*0.05*	790	*34*	7223	*112*
3	Exp3_MI_2	3.93	*0.05*	603	*34*	541	*8*
	Exp3_MI_6	4.09	*0.05*	3983	*164*	5462	*85*
4	Exp3_MI_3	4.46	*0.05*	8109	*339*	535	*8*
	Exp3_MI_1	1.64	*0.07*	113	*38*	79	*2*
	Exp3_tub_1	3.85	*0.05*	504	*32*	479	*7*
	Exp3_1	4.18	*0.17*				
	Exp3_2	4.29	*0.17*				
5	Exp3_3	3.84	*0.17*				
	Exp3_4	4.69	*0.17*				

678

679 Table 3. H_2O, CO_2 and F contents in re-homogenized inclusions measured by NanoSIMS.

Supplementary Information
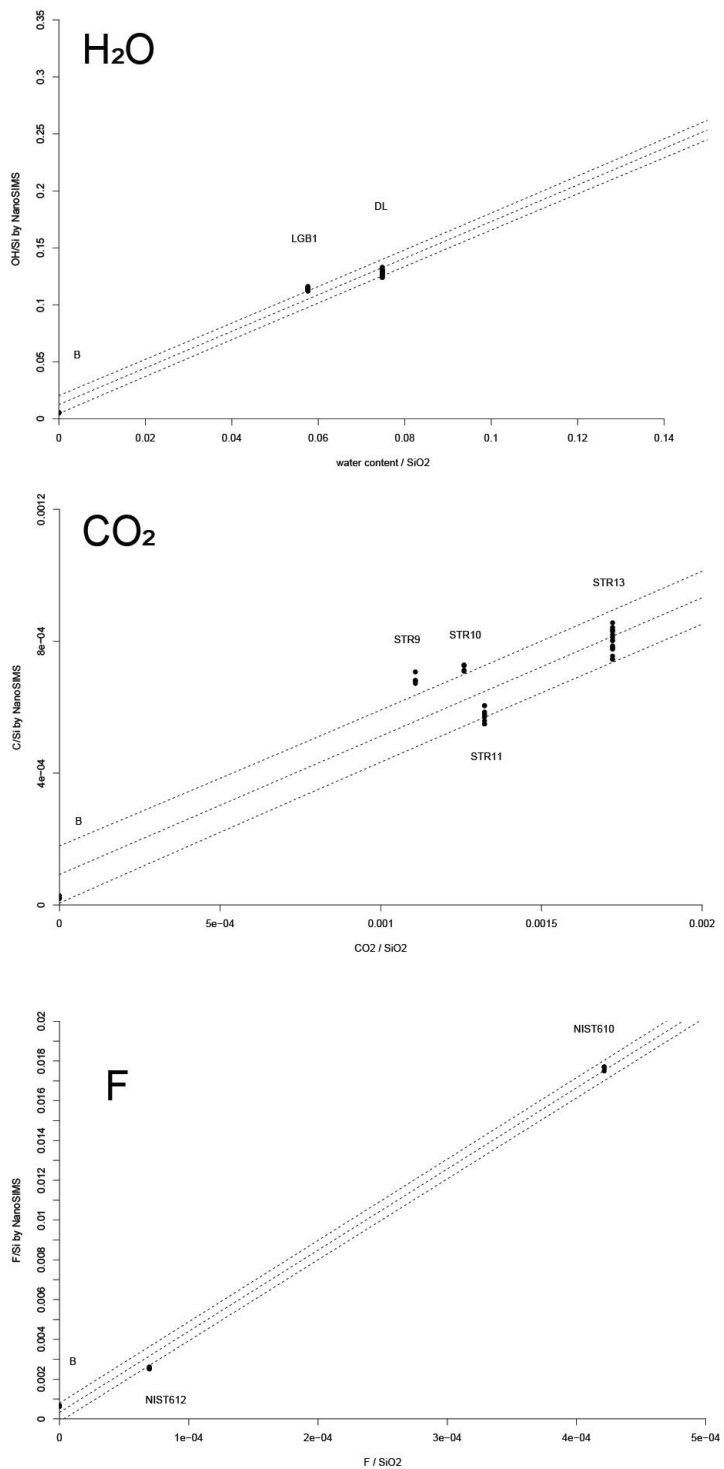
682   Figure S1. Calibration curves for NanoSIMS measurements.

Analyses	24	36	59	60	61	62	64
Duration	*24h*	*24h*	*24h*	*24h*	*24h*	*24h*	*24h*
T (°C)	*1050*	*1050*	*1050*	*1050*	*1050*	*1050*	*1050*
P (GPa)	*1.0*	*1.0*	*1.2*	*1.2*	*1.2*	*1.2*	*1.2*
Wt%							
SiO_2	56.42	57.42	56.95	56.52	52.89	56.33	52.55
TiO_2	0.78	0.00	0.01	0.13	0.00	0.39	0.05
Al_2O_3	14.75	18.67	13.87	16.58	13.89	14.77	15.49
FeO	12.01	11.13	7.45	6.71	9.86	11.41	14.91
MnO	0.11	0.11	0.04	0.02	0.09	0.14	0.08
MgO	1.24	4.67	2.78	3.17	2.94	3.28	4.36
CaO	2.66	0.99	0.86	1.55	1.05	1.34	1.26
Na_2O	3.43	1.08	1.08	1.33	0.89	1.23	0.88
K_2O	3.48	4.20	4.98	5.75	5.03	3.10	3.47
P_2O_5	1.72	0.12	1.78	0.04	0.12	0.16	0.16
Cl	0.07	0.21	0.08	0.86	0.82	0.68	0.93
Total	96.49	98.65	89.74	91.78	86.67	92.00	93.13

684

685   Table S1. EMP analyses of inclusions <5 μm in diameter.

686

687